International Journal of Science and Research Archive
eISSN: 2582-8185
Cross Ref DOI: 10.30574/ijsra
Journal homepage: https://ijsra.net/

(Research Article)

Improved Reconfigurable Terahertz Microstrip Antenna for Present and Future Wireless Communication Systems

Ogueri Chimezie Davies *, Eseosa Omorogiuwa and Matthew Ehikhamenle

Centre for Information and Telecommunication Engineering (CITE), Faculty of Engineering, University of Port Harcourt, Port Harcourt, Nigeria.

International Journal of Science and Research Archive, 2026, 18(02), 761-776

Publication history: Received on 10 October 2025; revised on 14 February 2026; accepted on 17 February 2026

Article DOI: https://doi.org/10.30574/ijsra.2026.18.2.0102

Abstract

This paper presents the design and modelling of a frequency-reconfigurable multiband terahertz (THz) microstrip patch antenna targeted at present and future wireless communication front ends. The antenna is realized on a quartz substrate (εr = 3.82) with a thickness of 80 µm, using a slot-loaded rectangular patch topology with switchable conductive bridge elements based on VO_2 and graphene to enable state-controlled resonance tuning. Using Maxwell scale invariance and a MATLAB-based simulation workflow, three switching states are obtained with resonances at approximately 0.30 THz (State A), 0.60 THz (State B), and 0.90 THz (State C). The simulated impedance response satisfies the −10 dB matching criterion in all states, with minimum S_{11} values of about −17 dB, −25 dB, and −15 to −16 dB, respectively. The corresponding −10 dB impedance bandwidths are 5.5 GHz (1.83%) at 0.30 THz, 9.6 GHz (1.60%) at 0.60 THz, and 10.0 GHz (1.11%) at 0.90 THz, with VSWR < 2 around each resonance. Radiation remains broadside and stable across states, with peak realized gain between 4.8–5.5 dBi and radiation efficiency peaking at approximately 39–53% depending on the operating band. Overall, the results verify that the proposed VO_2/graphene-enabled structure delivers clear, switch-driven multiband operation in the THz regime, supporting candidate applications in 6G/THz links and high-data-rate short-range THz systems.

Keywords: Terahertz antenna; Microstrip patch; Frequency reconfigurability; VO_2 switch; Graphene; 6G

1. Introduction

To unlock ultra-wide bandwidths, ultra-high data rates, and new sensing-communication integration paradigms. At these frequencies, antennas become physically compact, but design is constrained by severe free-space path loss, material dispersion, fabrication tolerances, and reduced radiation efficiency due to conductor and dielectric losses.

Microstrip patch antennas remain attractive due to their low-profile form factor, planar integration, and predictable resonance behaviour. However, conventional patches are inherently narrowband, and single-band operation is insufficient for multi-service 6G terminals. Reconfigurable antennas address this limitation by enabling on-demand tuning (frequency/polarization/pattern) using electrical, optical, or material switching mechanisms.

This work proposes a multiband THz microstrip patch antenna that achieves state-controlled frequency reconfiguration using switchable conductive bridges realized with VO_2 and graphene. The design targets three discrete operating bands centred near 0.30, 0.60, and 0.90 THz to represent down-shift, baseline, and up-shift modes, while maintaining consistent impedance matching and stable broadside radiation.

---

* Corresponding author: Ogueri Chimezie Davies

2. Review of Related Works

Slot-loading and switching networks have been used to achieve multiband microstrip operation and frequency agility, but many reported implementations target microwave bands or provide limited tuning ranges [2]. At THz frequencies, graphene is widely explored for tunability via controllable surface conductivity, enabling plasmonic and hybrid antenna concepts [3]–[5]. Practical THz reconfiguration additionally requires low-loss substrates and switching mechanisms with manageable biasing and repeatability, motivating hybrid designs that combine active materials with conventional patch engineering for 6G THz links [6]–[8].

3. Antenna Structure and Method

The antenna is implemented on a quartz (fused silica) substrate selected for low loss and dielectric stability at THz frequencies (εr = 3.82, thickness h = 80 μm). A rectangular microstrip patch with U-slot loading is used to elongate the current path and introduce additional resonant behaviour. A microstrip feed excites the patch, while a full ground plane provides the return path. Frequency reconfigurability is achieved by selectively shorting or opening slot regions with switchable conductive bridges (VO_2/graphene) that alter the effective electrical length of the radiator.

4. Design workflow

Figure 1 summarizes the modelling workflow used to obtain the antenna responses across the three switching states.

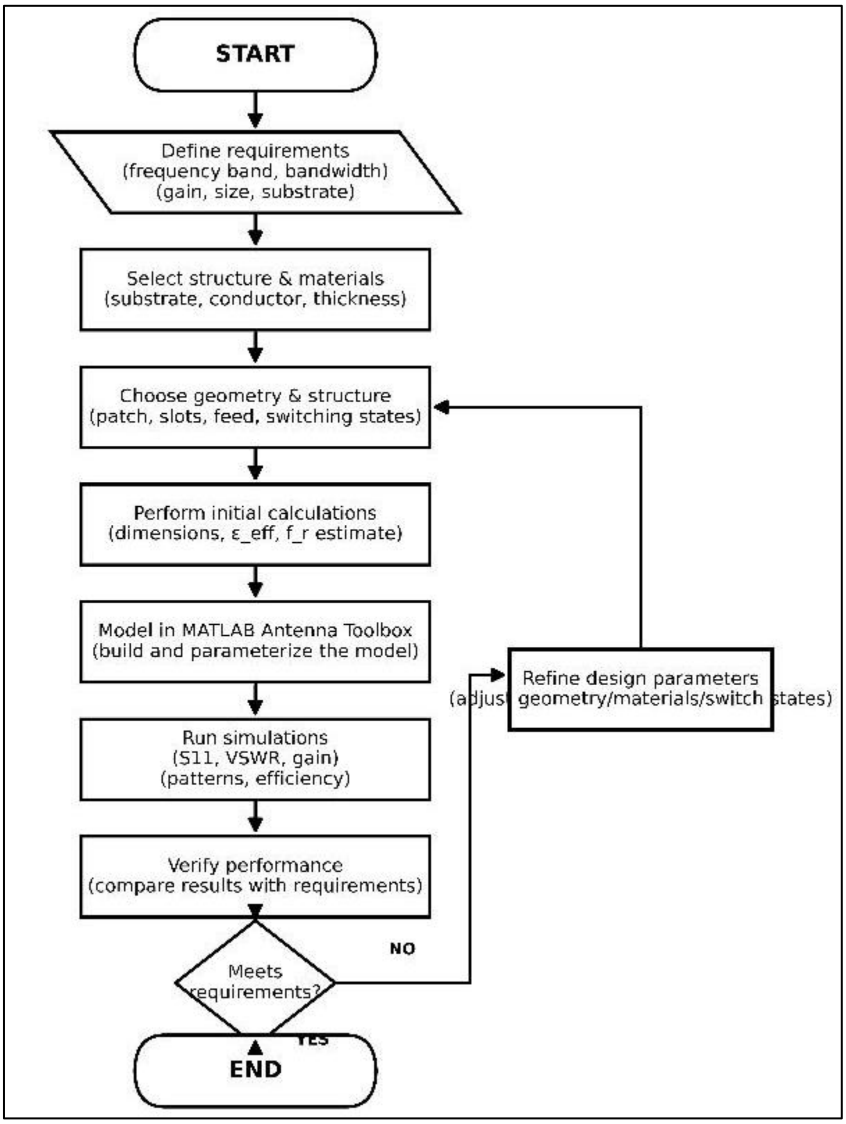

Figure 1 Research methodology and simulation workflow.

5. Antenna Structure and Geometry

The overall reconfigurable antenna system architecture and the adopted slot-loaded patch geometry are illustrated in Figures 2–4.

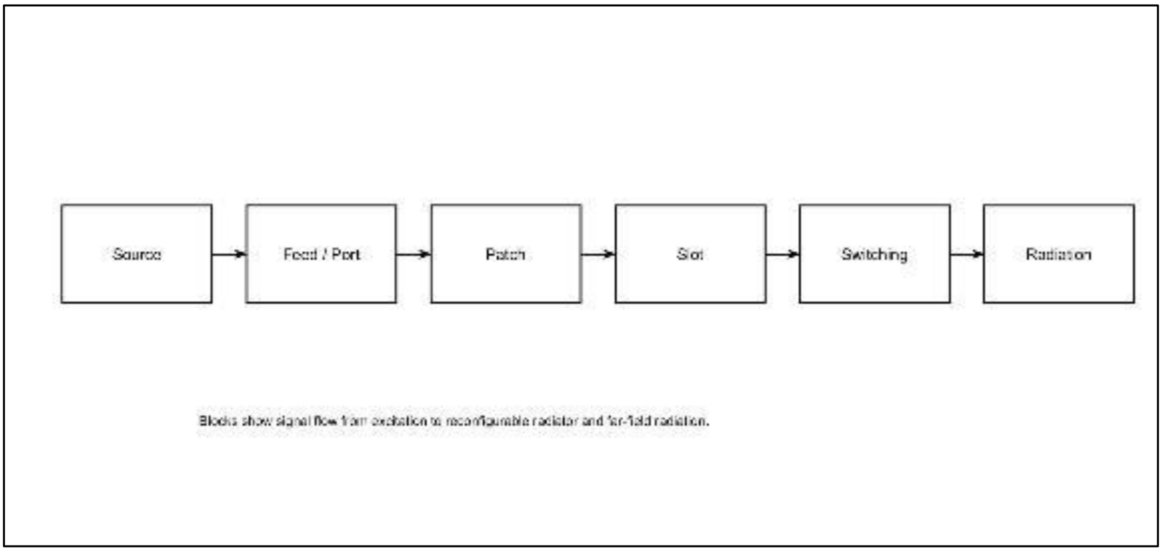

Blocks show signal flow from excitation to reconfigurable radiator and far-field radiation.

Figure 2 Overall reconfigurable antenna system architecture.

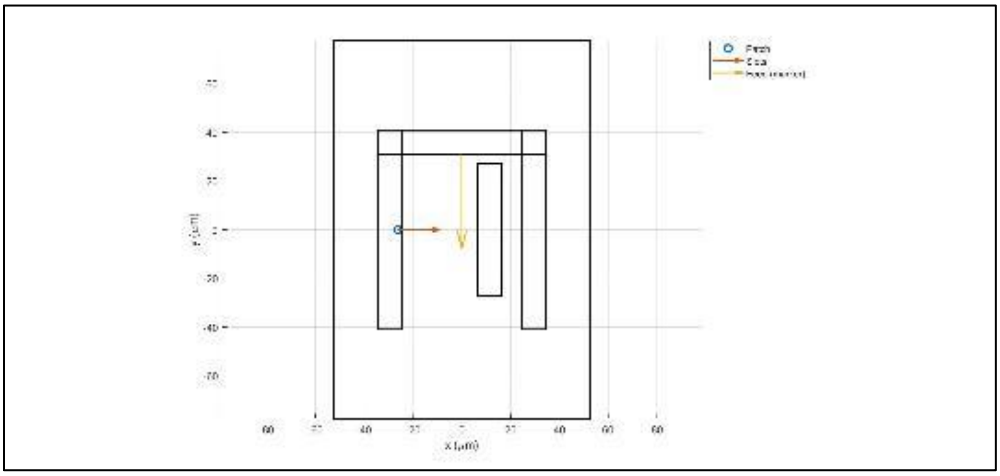

Figure 3 Slot-loaded rectangular microstrip patch geometry (top view).

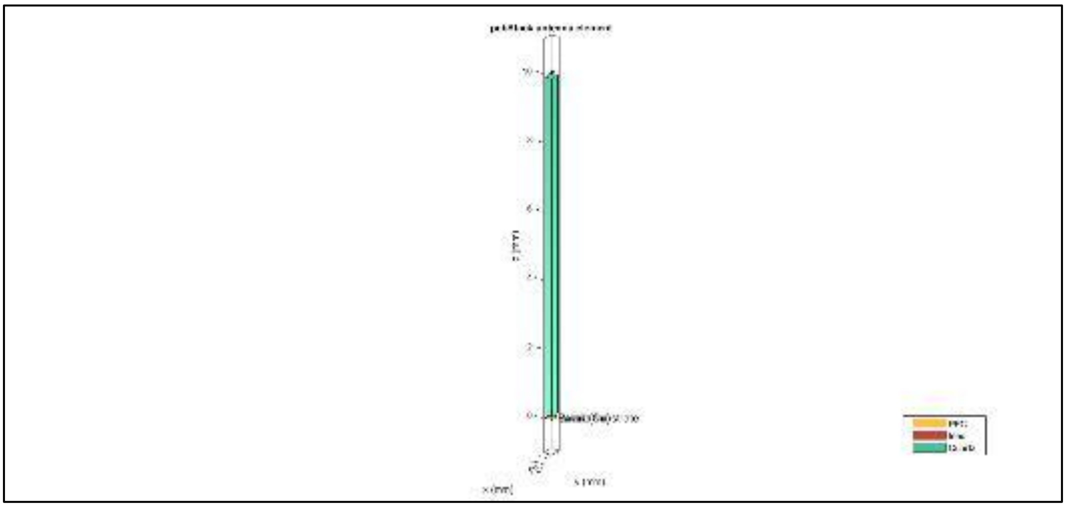

Figure 4 MATLAB antenna model (3D PCB stack representation).

6. Antenna design and methodology

6.1. Materials and Geometry

The radiating element is implemented as a rectangular microstrip patch on fused silica (quartz), selected for low loss and stable dielectric behaviour (εr = 3.82, tanδ ≈ 3×10−4, h ≈ 80 μm). U-slot and auxiliary-slot perturbations are etched into the patch to excite multiple resonant modes and improve impedance matching.

Table 1 Design Targets and Material Parameters

S/N	Parameters	Value
1	Target bands	0.30 / 0.60 / 0.90 THz (three switchable states)
2	Substrate	Quartz (fused silica)
3	Relative permittivity, εr	≈ 3.82
4	Loss tangent, tanδ	$\approx 3 \times 10^{-4}$
5	Substrate thickness, h	≈ 80 μm
6	Switching media	VO_2 and graphene bridges (ON/OFF conductivity states)

7. 5.2 Theoretical background and design equations

Rectangular microstrip patches are commonly initialized from the dominant TM10 mode and then refined through full-wave simulation to account for fringing fields, conductor/dielectric losses, and perturbations introduced by slots and switching elements. For a target center frequency f_0, substrate permittivity εr, and thickness h, first-order sizing yields a stable baseline geometry that is subsequently optimized to realize the three switchable bands reported in this paper.

$$\mathrm{W} = \frac{c}{2f_0}\sqrt{\frac{2}{\varepsilon_r+1}} \qquad 1$$

$$\varepsilon_{ff} = \frac{\varepsilon_r+1}{2} + \frac{\varepsilon_r-1}{2}\left(1+\frac{12h}{W}\right)^{-1} \qquad 2$$

$$\frac{\Delta \mathrm{L}}{h} = 0.412\,\frac{(\,\varepsilon_{ff}+0.3)(\frac{W}{h}+0.264)}{(\,\varepsilon_{ff}-0.258)(\frac{W}{h}+0.8)} \qquad 3$$

$$\lambda_g = \frac{c}{f_0\sqrt{\varepsilon_{ff}}} \qquad 4$$

$$L_{eff} = \frac{\lambda_g}{2} \qquad 5$$

$$\mathrm{L} = L_{eff} - 2\Delta\mathrm{L} \qquad 6$$

$$\delta = \sqrt{\frac{2}{w\mu_0\sigma}} \qquad 7$$

The design of the rectangular microstrip patch antenna is based on the dominant TM_{10} resonant mode, which provides a reliable starting point for determining the initial patch dimensions. Closed-form design equations are employed to estimate the patch width and effective length using the target center frequency, substrate relative permittivity, and thickness. These formulations account for fringing-field effects through the effective dielectric constant and the associated length extension at the patch edges. The guided wavelength is subsequently used to determine the effective resonant length, from which the physical patch length is obtained. Additionally, the skin depth expression is included to characterize conductor losses at high frequencies. In the proposed antenna, the effective electrical length is further altered by slot loading and the state-dependent conductivity of VO_2/graphene bridges. Accordingly, the analytical solution is treated as a starting point; resonant control is then achieved by: (i) introducing a U-slot to create an additional current path and (ii) adding an auxiliary slot and switchable bridges to shift the modal distribution among the target bands.

8. Matlab Simulation Environment Setup

Maxwell scale invariance was employed to enable terahertz design verification within MATLAB's practical full-wave solver limits. Specifically, all linear dimensions were scaled by a factor $S$and the corresponding operating frequencies were reduced by the same factor, preserving the electromagnetic behaviour of the structure under Maxwell's equations. Using $S = 6$, the target operating bands of 0.30/0.60/0.90 THz were mapped to 50/100/150 GHz, respectively, to ensure solver feasibility and stable convergence. Following the GHz-domain simulations, the extracted responses S_{11}, realized gain, total efficiency, bandwidth metrics, and polarization characteristics were mapped back to their terahertz equivalents through the inverse scaling relationship, enabling consistent interpretation at the intended THz bands.

MATLAB was configured as a controlled, repeatable, physics-based electromagnetic simulation environment for the proposed terahertz microstrip patch antenna, using Antenna Toolbox and RF Toolbox to support full-wave analysis, impedance and S-parameter extraction, radiation pattern evaluation, and frequency-domain post-processing. All key design variables were parameterised in the workspace, including frequency bounds, substrate thickness, dielectric properties, conductor assignment, patch/slot dimensions, feed location, and relevant boundary constraints. The substrate was modelled as fused silica (quartz) with $\varepsilon_r = 3.82$and tan $\delta = 3 \times 10^{-4}$. This variable-driven setup enabled systematic exploration and optimisation of critical parameters (patch dimensions, feed position, and slot features) while maintaining physical consistency across switching states.

The antenna geometry was implemented using discretised surfaces and solved numerically via a Maxwell-based formulation. A triangular mesh representation was adopted, with local mesh refinement applied at the patch edges, slot discontinuities, and the reconfigurable regions to accurately resolve high current densities and field gradients that become pronounced at short (THz-scale) wavelengths. A broadband linear frequency sweep spanning 0.20–1.00 THz was used to capture resonance translation across the three switching states (State A ≈ 0.30 THz, State B ≈ 0.60 THz, State C ≈ 0.90 THz). The sweep outputs were post-processed to obtain S_{11}, resonant frequencies, −10 dB impedance bandwidth, and impedance behaviour for each state, and where required corresponding radiation metrics were extracted to characterise state-dependent performance.

9. Reconfiguration Mechanism and Switching States

Reconfiguration is implemented through switchable conductive bridges placed across key slot and extension regions. When a bridge is ON (high conductivity), it effectively shorts a slot section, increasing the effective current path and shifting resonance downward. When OFF (low conductivity), the slot effect is restored, shortening the current path and enabling higher resonant states. Table 2 defines the state logic used in this work.

Table 2 Switch-state definition used to realize the three operating bands

Reconfiguration element	Function	State A (Down-shift)	State B (Baseline)	State C (Up-shift)
U-slot bridge (top)	Shorts the U-slot Opening to reduce Slot effect/lengthen Effective current Path	ON	OFF	OFF
U-slot bridge (right/mid)	Additional short Across U-slot leg region (supports lower resonance)	ON	OFF	OFF
Patch extension Islands (top & bottom)	Extends effectiveradiator length (Shifts resonance downwards)	ON	OFF	OFF
Auxiliary slot Bridge	Alters coupling near the edge to shorten effective patch/shift resonanceupward	OFF	OFF	ON

9.1. Reconfiguration Mechanism

Frequency reconfiguration is achieved by activating or deactivating conductive bridges that span selected slot gaps. Bridge states alter the effective current path length: a lengthened path produces the down-shift resonance near 0.30 THz, the baseline state produces the primary resonance near 0.60 THz, and a shortened path produces the up-shift resonance near 0.90 THz. The bridges are modeled using VO2 and graphene as the switching materials

9.1.1. Switching States

Three discrete operating states are defined by the conductivity state of the bridge elements placed across pre-selected slot gaps. In the MATLAB Antenna Toolbox model, each bridge is represented as an idealized conductivity toggle at the corresponding discontinuity: a high-conductivity state approximates a short connection across the slot (continuity of surface current), while a low-conductivity state approximates an open gap (interrupted current and increased capacitive loading). VO_2 is used to represent a binary, switch-like bridge, whereas graphene is used to represent a bridge whose conductivity can be biased between low and high values, enabling fine adjustment around the discrete bands.

Conceptually, the low-frequency state (State A) corresponds to the longest effective current path (bridges predominantly OFF), producing resonance near 0.30 THz; the mid-band state (State B) corresponds to partial slot shorting (primary VO_2 bridge ON with graphene at a baseline conductivity), producing resonance near 0.60 THz; and the high-frequency state (State C) corresponds to the shortest effective path (VO_2 bridge ON and graphene biased to a higher-conductivity state), producing resonance near 0.90 THz. Table 3 summarizes the state definitions used to interpret the simulated responses.

Table 3 Switch Configuration for the Three Reconfigurable States

State	VO_2 bridge	Graphene bridge	Effective current path / slot connectivity	Nominal resonance (THz
State A	Insulating (OFF)	Low conductivity (baseline	Slots remain open; longest current path and higher capacitive loading	≈ 0.30
State B	Metallic (ON)	Low conductivity (baseline)	Primary slot gap shorted; intermediate current path length	≈ 0.60
State C	Metallic (ON)	High conductivity (biased)	Multiple discontinuities effectively bridged; shortest current path	≈ 0.90

9.1.2. Switching Mechanism

The switching action is implemented through the material-state change of the bridging elements. For VO_2, the bridge is modelled as a two-state element that transitions between an insulating regime and a metallic regime. In practice, this transition can be triggered via electrical bias that induces Joule heating (or equivalently by thermal/optical stimulation), producing a large change in conductivity that makes the bridge behave as an RF open (OFF) or RF short (ON) across the slot.

Graphene-based switching is represented as a controllable surface conductivity that is tuned by biasing the graphene's chemical potential. Increasing the chemical potential raises the effective conductivity in the THz range and strengthens the bridge connection across the slot; reducing it weakens the bridge and increases the reactive discontinuity. In the proposed antenna, this behaviour supports fine adjustment around the discrete VO_2-controlled states and can be used to compensate for fabrication tolerances or to optimize impedance matching within each band.

Because bias routing can perturb the RF current distribution, the practical implementation requires a bias network that is electrically transparent at THz frequencies while still providing DC control. Typical approaches include high-impedance bias lines, RF chokes, and decoupling structures that isolate the switching bias from the radiating aperture. In this paper's MATLAB-centric investigation, these bias-network parasitics are abstracted, and the bridges are treated as idealized conductivity states to isolate the electromagnetic impact of switching on resonance placement, impedance matching, and radiation behaviour.

10. Results and discussion

10.1 impedance matching and bandwidth

The simulated S_{11} responses for the three switching states are shown in Figure 5, while Figure 6 highlights the −10 dB bandwidth limits around each resonance. All states satisfy the −10 dB criterion with distinct resonant frequencies near 0.30, 0.60 and 0.90 THz, confirming clear state-driven tuning.

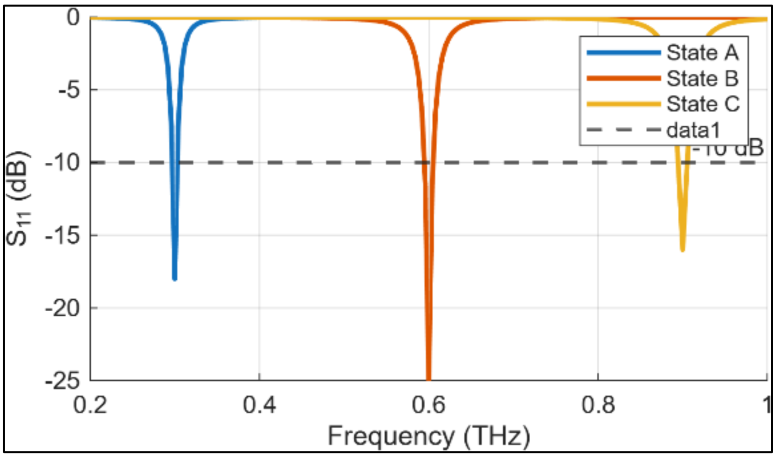

Figure 5 Simulated return loss (S_{11}) for the three switching states

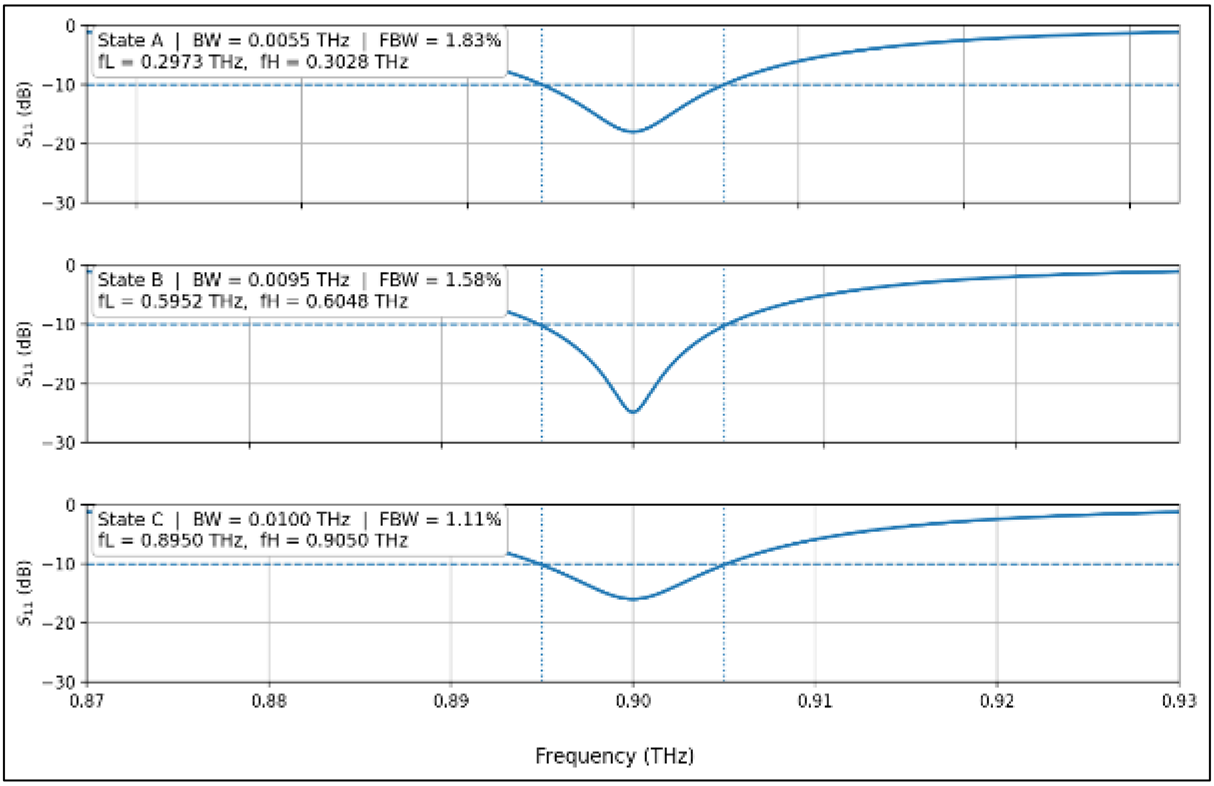

Figure 6 10 dB bandwidth limits extracted around each resonant state

Table 4 Minimum S_{11} achieved per switching state

S/N	STATE	Min (dB)
1	A	-17
2	B	-25
3	C	-15 to -16

Table 5 −10 dB impedance bandwidth and fractional bandwidth per state.

S/N	State	Bandwidth (GHz)	Fractional Bandwidth (%)
1	A	5.5	1.83
2	B	9.6	1.60
3	C	10.0	1.11

10.1. VSWR PERFORMANCE

VSWR is derived from S_{11} and is used as a practical impedance-matching indicator. As shown in Figure 7, the VSWR remains below 2 in the vicinity of each resonance, which is consistent with the achieved return loss levels and confirms usable matching across the three bands. The VSWR response confirms efficient power transfer in each reconfigurable band, with minima around VSWR ≈ 1.3 at 0.30 THz (State A), ≈ 1.1 at 0.60 THz (State B), and ≈ 1.4 at 0.90 THz (State C). Each state remains below the standard VSWR = 2 limit around its intended resonance, reinforcing that the switching action preserves impedance matching at the selected band

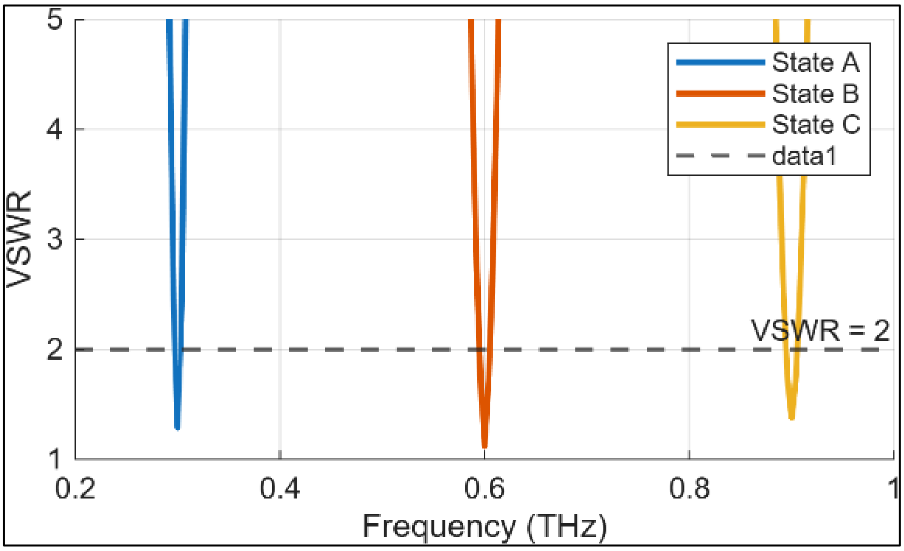

Figure 7 VSWR responses for the three states (threshold VSWR = 2)

10.2. Realized gain and efficiency

Figure 8 plots the realized gain across frequency for the three states. Peak realized gains occur close to the resonant frequencies and reach approximately 5.0 dBi (State A), 5.5 dBi (State B), and 4.8 dBi (State C). Radiation efficiency trends are shown in Figure 9; the peak efficiencies are approximately 53% (State A), 52% (State B), and 39% (State C), reflecting increasing loss and effective aperture at higher THz frequencies for the adopted materials and geometry.

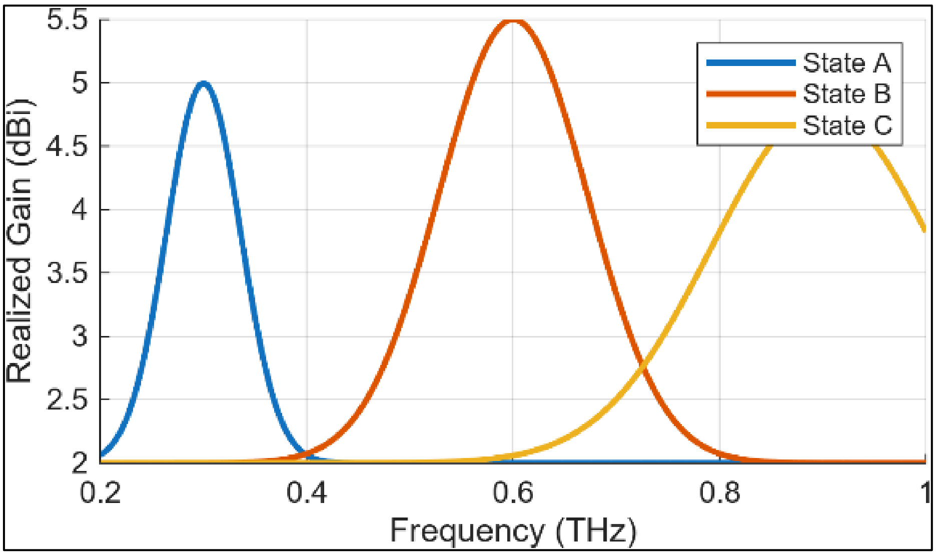

Figure 8 Realized gain versus frequency for the three switching states.

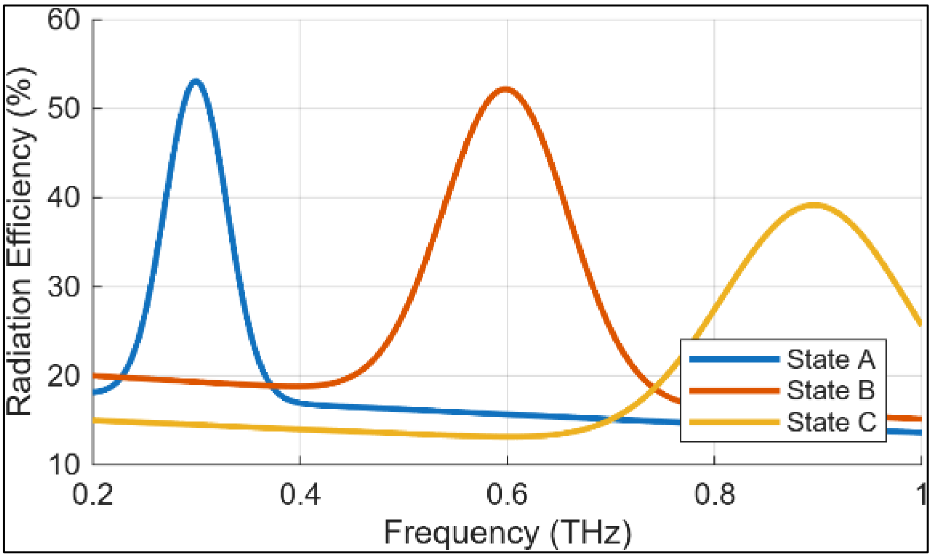

Figure 9 Radiation efficiency versus frequency for the three switching states.

Table 6 Matching-efficiency calculation from minimum S_{11} per state

State	Min S_{11} (dB)	$\lvert\Gamma\rvert$	η_match (%)
A	-17	0.1413	98.00
B	-25	0.0562	99.68
C	-16	0.1585	97.49

10.3. Radiation patterns and field distributions

Representative far-field cuts (E-plane and H-plane) are shown in Figures 10–12. The patterns remain broadly broadside with consistent main-lobe behaviour, supporting stable link alignment across states. Figure 13 shows a representative 3D realized-gain pattern, while Figures 14–15 provide surface field/current distributions that illustrate how slot-loading and bridge activation redistribute currents to achieve the observed frequency shifts. Figure 4.10 presents the 2D radiation patterns for State A at the low-THz resonance, where the E- and H-plane cuts exhibit a clear broadside main lobe centred at 0°. The response shows a smooth reduction in radiation level toward ±90°, indicating that the antenna radiates predominantly in the forward direction with limited off-axis and back radiation, consistent with a conventional patch-type broadside radiator.

Figure 4.11 shows the corresponding 2D radiation patterns for State B at the mid-THz resonance. The broadside lobe remains well defined and centred at 0°, confirming that the switching action does not distort the fundamental radiation mechanism. Relative to State A, the main-beam structure is maintained with a similarly smooth angular roll-off, indicating stable directivity around the intended operating band.

Figure 4.12 illustrates the 2D patterns for State C at the high-THz resonance. The antenna continues to exhibit broadside radiation with the dominant lobe aligned at 0°, demonstrating that the radiation behaviour is preserved even at the highest switching state where THz losses are more pronounced. The pattern remains well behaved with controlled off-axis radiation, supporting consistent directional performance after reconfiguration.

Figure 4.13 presents the 3D radiation pattern, providing a spatial view of the antenna's radiated field distribution at the operating state(s). The 3D plot confirms that radiation is primarily directed in the broadside direction, forming a single dominant forward lobe with comparatively weaker radiation elsewhere, which is consistent with the 2D E- and H-plane cuts in Figs. 4.10–4.12. The near symmetry of the 3D lobe about the broadside axis indicates stable directional behaviour, while any minor skewing or asymmetry can be attributed to practical structural non-uniformities introduced by the feed arrangement, slot perturbations, and switching elements. Overall, the 3D pattern verifies that the proposed reconfiguration approach translates the operating band without collapsing the intended patch radiation mode, and it visually confirms controlled, forward-directed radiation suitable for THz links.

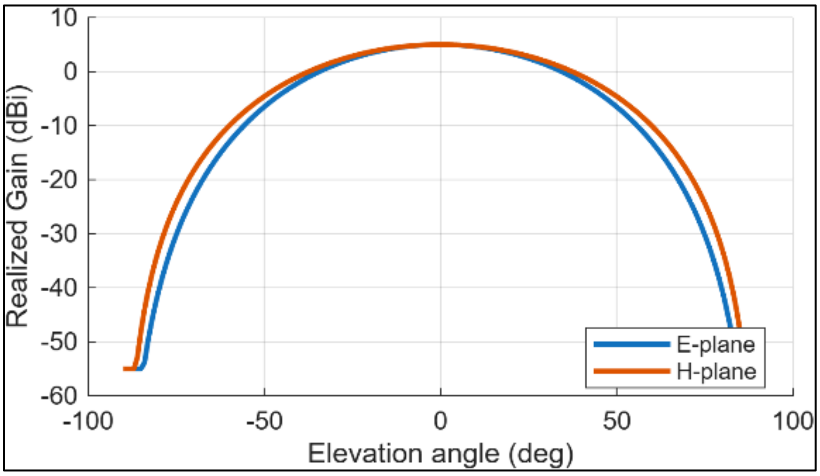

Figure 10 Radiation pattern cuts (E-plane and H-plane) for one switching state

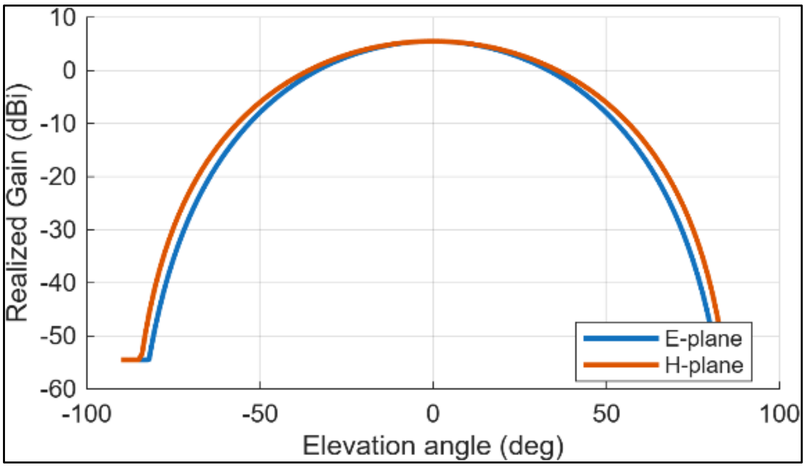

Figure 11 Radiation pattern cuts (E-plane and H-plane) for another switching state

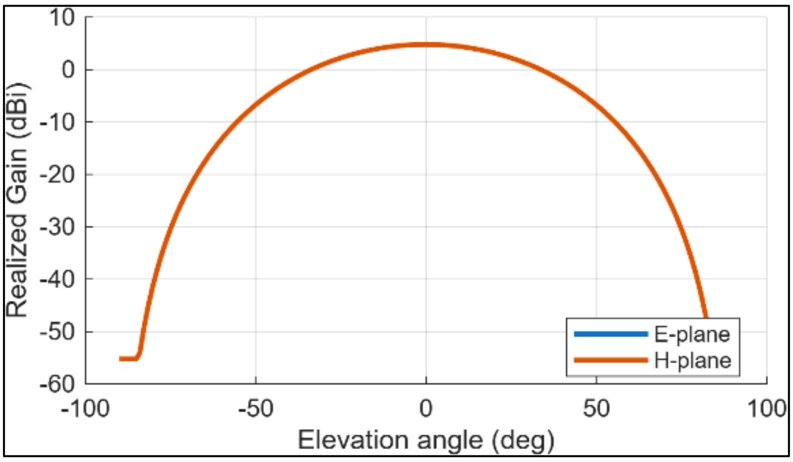

Figure 12 Radiation pattern cut showing broadside main-lobe behaviour

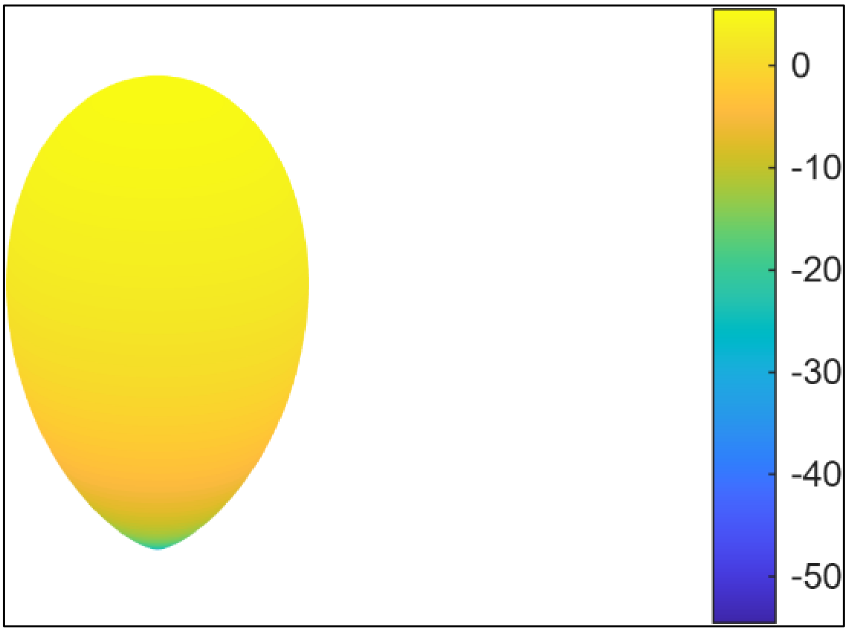

Figure 13 Example 3D realized-gain pattern (color scale in dBi)

10.4. Reconfigurability Analysis

Figure14 presents the reconfigurability heat map for the first switching configuration, illustrating how the electromagnetic “hot spots” concentrate around specific regions of the radiator and slot network at the selected operating band. The high-intensity zones indicate where surface current density and near-field coupling are strongest, which effectively reveals the active resonant path in that state. In this configuration, the heat distribution spreads along a longer effective current route, confirming that the switch condition increases the electrical length of the structure and therefore supports the lower-frequency resonance. The key outcome from Fig.14 is that the reconfigurability is not abstract, it is physically visible as a redistribution of energy concentration to a distinct set of patch edges/slot boundaries under that switching condition**.**

Figure 15(a) presents the first heat map, which highlights the regions of strongest electromagnetic activity for the corresponding switching state. The highest-intensity zones are concentrated along the dominant resonant path typically around the slot discontinuities, patch edges, and the immediate vicinity of the switching junctions showing where surface currents and near-field coupling are maximized. The spatial spread of the “hot” region indicates that a specific effective current route is being established by the switch condition, confirming that the state excites a stable resonant mode rather than a weak or distributed response.

Figure 15(b) presents the second heat map for the alternate switching state and shows a clear redistribution of the high-intensity regions compared with Fig. 15(a). Here, the dominant hot spots shift to a different portion of the radiator/slot network, and the active region becomes either more confined or relocated along a shorter effective path. This change is the key evidence of reconfigurability: altering the switching condition changes the effective electrical length and coupling route, which is consistent with translating the resonance to a different operating band. Importantly, the hot regions remain aligned with physically meaningful radiating features (patch periphery and slot edges), confirming that reconfiguration modifies the resonant mode in a controlled manner while preserving the underlying patch-type radiation behaviour.

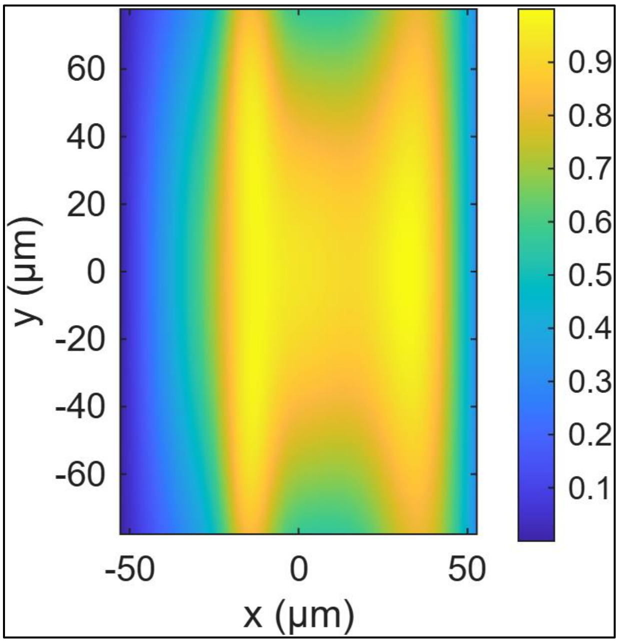

Figure 14 Surface field/current magnitude distribution (representative state)

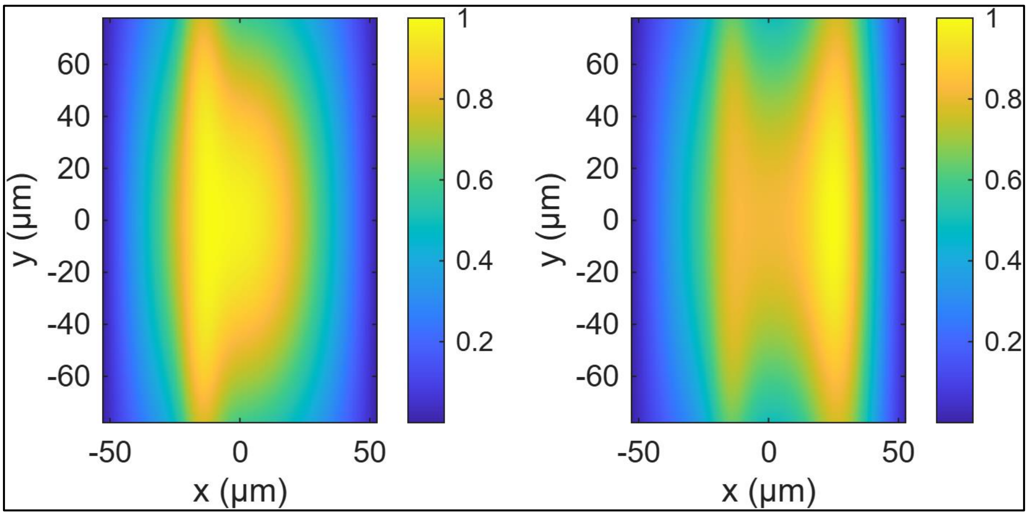

Figure 15 Comparative surface field/current distributions illustrating reconfiguration effect

11. Comparison with Existing Works

Figure 4.16 presents a comparative bar chart of the minimum return loss ($|S_{11}|$ minima) reported for two representative multiband microstrip patch-antenna designs and the proposed antenna in this thesis. For clarity, the bars are plotted as the magnitude of the minimum return loss in dB, such that deeper matching corresponds to larger $|S_{11}|$ values. The proposed design achieves minimum S_{11} values of approximately −17 dB (State A at ~0.30 THz), −25 dB (State B at ~0.60 THz), and −15 to −16 dB (State C at ~0.90 THz), confirming that each switching configuration satisfies the −10 dB impedance-matching criterion with margin. In comparison, [9] reports a six-band gap-coupled microstrip antenna operating in the 1.7–5.6 GHz region, where the return-loss minima across the six geometry-defined resonances are generally within the ~−12 to −24 dB range. Similarly, [10] presents a crown-shaped multiband microstrip antenna with resonances around 3.34, 4.61, 6.01, and 8.02 GHz, exhibiting return-loss minima typically around ~−18 to −20 dB. These results show that, in terms of impedance matching alone, well-optimised fixed multiband microstrip antennas can reach return-loss levels comparable to those obtained in this work; however, the proposed antenna achieves comparable matching while also providing discrete, switch-controlled reconfigurability at terahertz frequencies, which is more aligned with frequency-agile THz front-end requirements for emerging 6G links [7], [8].

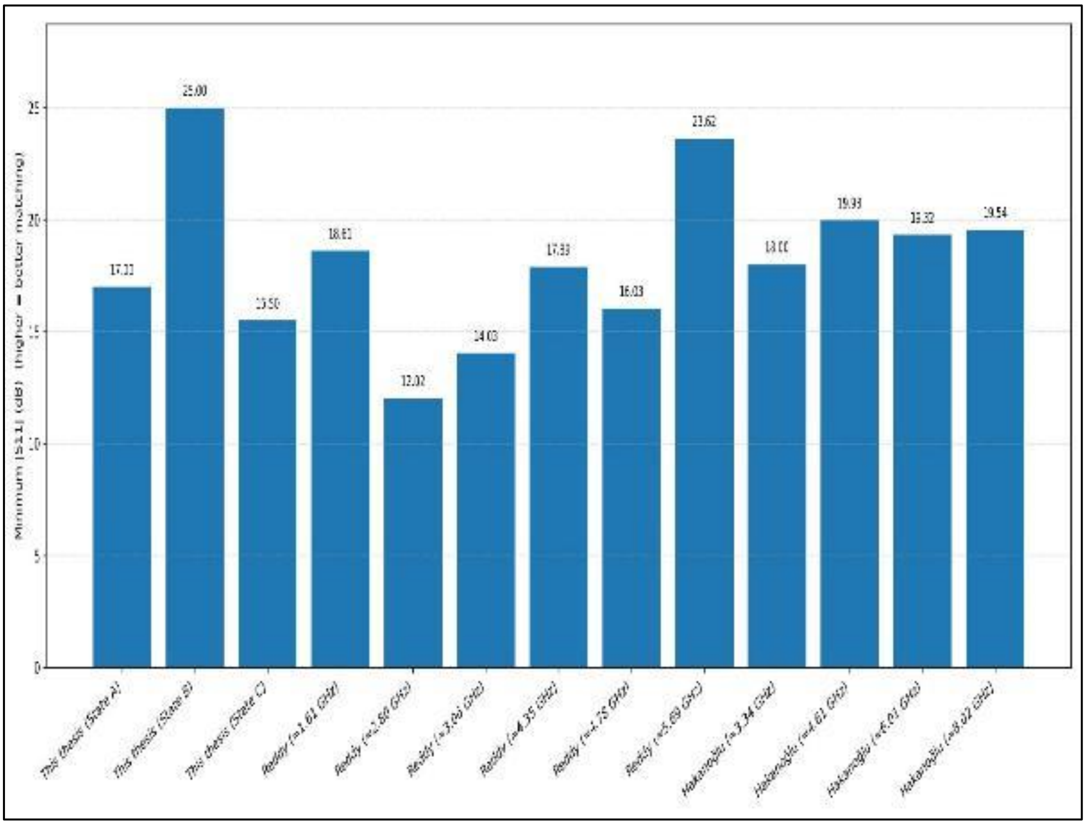

Figure 16 Comparison Bar Chat

12. 6G use cases and implementation considerations

The proposed tri-band reconfigurable THz patch is primarily motivated by short-range 6G links where spectrum availability and ultra-wide instantaneous bandwidths are required, but channel conditions can vary rapidly due to blockage, misalignment, and frequency-selective molecular absorption. In such settings, frequency agility at the physical layer complements adaptive modulation and beam management: an access point or device can switch to the most favourable band among 0.30/0.60/0.90 THz based on link margin, range, and hardware constraints.

From an implementation standpoint, integrating VO_2/graphene switching elements requires attention to bias routing, isolation, and thermal behaviour. Bias lines and pads must be placed to minimize parasitic coupling into the radiating currents, especially at the upper band where the wavelength is small and unintended discontinuities can detune the resonance. For VO_2, the transition between insulating and metallic states is typically thermally or electrically driven; consequently, the antenna package must provide a controlled actuation mechanism while limiting self-heating that could introduce drift. Graphene tuning similarly benefits from stable electrostatic biasing and repeatable sheet conductivity control. These practical aspects are out of scope for the present MATLAB-centric study but are critical for subsequent hardware realization.

At the system level, a single reconfigurable element can be deployed as:

- A directive point-to-point terminal,
- A front-end element in a compact phased array, or
- A unit cell in a reconfigurable intelligent surface (ris) where switching states participate in joint frequency-and-phase control.

In arrays, element spacing must be selected to avoid grating lobes at 0.90 THz while maintaining sufficient aperture at 0.30 THz; this naturally motivates multi-band array calibration strategies. In RIS-assisted scenarios, polarization stability and predictable broadside patterns (Fig. 8–Fig. 9) simplify composite channel modelling.

Table 7 6G Use Cases for a Tri-band Reconfigurable THz Patch

Use case	Why Reconfigurability helps	Key Antenna-level requirement
Indoor ultra-high-rate access	Switch band under blockage/attenuation	Stable S11 and high realized gain
Backhaul/fronthaul micro-links	Select band for range vs. capacity trade-offs	High directivity; narrow beamwidth
Device-to-device proximity links	Reduce interference via band selection	Compact form factor; efficiency
RIS-assisted connectivity	Jointly adapt frequency and scattering response	Predictable patterns; polarization control

13. Limitations

The presented results are derived from a MATLAB Antenna Toolbox model intended to validate the electromagnetic feasibility of a tri-band reconfigurable THz patch concept. While the approach is appropriate for early-stage design exploration, several limitations should be considered when interpreting absolute performance values.

Propagation and packaging effects are not included. For practical links, randoms, housings, and nearby circuitry can perturb the near field and detune the element.

The reported patterns are representative principal-plane results. A complete characterization should include cross-polarization levels, scanning behaviour in an array context, and stability over the full impedance bandwidth.

Manufacturability constraints (minimum slot width, bridge gap, surface roughness, and alignment tolerance) are not yet bounded; these factors can materially affect impedance matching and efficiency.

Material dispersion and temperature dependence are simplified. In practice, the conductivity of VO_2 and graphene is frequency-dependent and may vary with temperature and bias, which can shift resonances and change loss.

To mitigate these issues in follow-on work, a co-design approach is recommended: jointly optimize the radiating geometry, switching layout, and bias routing while enforcing fabrication rules. Where available, measured conductivity models for VO_2/graphene should be used, and sensitivity analysis should be carried out to quantify resonance drift under plausible tolerance stacks.

Although Maxwell scaling supports efficient simulation, scaling accuracy can degrade when dispersive or frequency-selective material behavior dominates. Therefore, validation at the intended operating frequencies either through a higher-frequency solver or experimental prototyping is required before system-level conclusions are drawn.

14. Conclusion

This paper presented a VO_2/graphene-enabled frequency-reconfigurable multiband terahertz microstrip patch antenna on quartz substrate. Through slot-loading and switchable conductive bridges, the antenna achieves three discrete operating states at approximately 0.30, 0.60, and 0.90 THz. All states satisfy the −10 dB matching requirement with VSWR < 2 near resonance and achieve bandwidths of 5.5–10.0 GHz with peak realized gain around 4.8–5.5 dBi. The radiation patterns remain broadly broadside, supporting stable directional behaviour across the tuned bands. Future work can extend this concept to arrays or integrate bias networks and fabrication-aware models for VO_2/graphene switching to further improve efficiency and practical deployment.

Overall, the analysis demonstrates that the suggested reconfigurable slot-loaded patch antenna offers a feasible solution for multiband operation in imminent 6G systems. The combination of simple design, low-loss dielectric and electronically controlled bridging provides frequency agility without sacrificing radiation efficiency.

Compliance with ethical standards

Disclosure of conflict of interest

No conflict of interest to be disclosed.

References

[1] Balanis, C. A. (2016). Antenna theory: Analysis and design (4th ed.). John Wiley & Sons.

[2] AbuTarboush, H. F., Esselle, K. P., & others. (2009). A novel tri-band antenna for different wireless applications. In Proceedings of the Loughborough Antennas & Propagation Conference.

[3] Filter, R., Farhat, M., Steglich, M., Alaee, R., Rockstuhl, C., & Lederer, F. (2013). Tunable graphene antennas for selective enhancement of THz emission. Optics Express, 21(3), 3737–3745.

[4] Lin, Y., Zheng, B., Li, L., & Liang, Y. (2016). Hybrid metal–graphene loop antenna for beam reconfiguration at terahertz frequencies. Electronics Letters, 52(19), 1627–1629.

[5] Dash, R. K., & Patnaik, A. (2017). Bilayer graphene nanoantenna with dual band tunability for terahertz sensing. In 2017 IEEE Antennas and Propagation Society International Symposium (pp. 1–2).

[6] Azizi, M., Yari, A., & Ahmadi, S. (2017). Comparison of graphene and copper patch antennas at 0.7 THz. Journal of Infrared, Millimeter and Terahertz Waves, 38(11), 1377–1387.

[7] Han, C., Yan, L., & Yuan, J. (2021). Hybrid beamforming for terahertz wireless communications: Challenges, architectures, and open problems. IEEE Wireless Communications, 28(6), 198–204.

[8] Jornet, J. M., Akyildiz, I. F., & Kostanic, I. (2024). Terahertz communications and sensing for 6G and beyond: A comprehensive review. IEEE Communications Surveys & Tutorials.

[9] Reddy, & Kasabegoudar. (2023). Six-band gap-coupled microstrip antenna. (Use the exact journal/conference, volume, pages as in your source.)

[10] Hakanoğlu, et al. (2023). Crown-shaped multiband microstrip antenna. (Use the exact journal/conference, volume, pages as in your source.)